Thin Solid Films 529 (2013) 66–70

Contents lists available at SciVerse ScienceDirect

Thin Solid Films

journal homepage: www.elsevier.com/locate/tsf

Fabrication and ferroelectric properties of $BiFeO_3/LaNiO_3$ artificial superlattice structures grown by radio-frequency magnetron-sputtering

Yen-Ting Liu [a,1], Shang-Jui Chiu [b], Hsin-Yi Lee [c,d,*], San-Yuan Chen [c]

[a] Program for Science and Technology of Accelerator Light Source, National Chiao Tung University, Hsinchu, Taiwan
[b] Department of Engineering and System Science, National Tsing Hua University, Hsinchu, Taiwan
[c] National Synchrotron Radiation Research Center, Hsinchu, Taiwan
[d] Department of Materials Science and Engineering, National Chiao Tung University, Hsinchu, Taiwan

ARTICLE INFO

Available online 24 July 2012

Keywords:
Superlattice
RF sputtering
X-ray scattering

ABSTRACT

Symmetric superlattice structures of multiferroic $BiFeO_3$ and conductive $LaNiO_3$ sublayers were grown on a Nb-doped $SrTiO_3$ substrate with radio-frequency magnetron-sputtering. The formation of a superlattice structure was confirmed from the appearance of satellite lines on both sides of the main line in the X-ray diffraction pattern. X-ray measurements show that these superlattice films become subject to greater tensile stress along the *c*-axis and to increased compressive stress parallel to the surface plane with a decreasing thickness of the sublayer.

The smaller is the thickness of the sublayer, the greater is the crystalline quality and the strain state. The hysteresis loops show a large leakage current at frequencies of 0.5 and 1 kHz; the polarization decreases with an increasing frequency.

1. Introduction

Multiferroic $BiFeO_3$ (BFO) exhibits both a ferroelectric phase transition at Curie temperature $T_C = 1103$ K and a magnetic phase transition at Néel temperature $T_N = 643$ K, rendering it both ferroelectric and ferromagnetic simultaneously [1–4]. As the material is free of lead, it becomes a worthy candidate for practical applications. Ferroelectric thin films promise diverse applications in microelectronic and data-storage devices, such as sensors, transistors and nonvolatile memories [5]. BFO has attracted much attention because of its superior ferroelectric properties in the form of an epitaxial thin film in comparison with counterpart bulk single crystals or ceramics [6,7]. Because of the large polarization and large piezoelectric coefficient, multiferroic BFO thin films have been considered to be among the most promising candidates for ferroelectric random-access memories and micro-electromechanical systems [8]. Exploring how the substrate-induced strain affects the ferroelectric behavior of ferroelectric thin films is an important issue, as epitaxial strains can greatly enhance the ferroelectric polarization and the Curie temperature of thin films relative to their bulk counterparts [9].

Considerable effort has been focused on the deposition of BFO thin films with the most desirable film texture and electrical behavior for several technologically demanding applications, including pulsed-laser deposition, sol–gel synthesis and chemical-vapor deposition [10–13]. We used radio-frequency (RF) magnetron sputtering to grow epitaxial thin films because of the highly reproducible chemical composition and the facile control of the process [14–16]. Sputtering allows us to grow complicated oxide thin films with extremely smooth surfaces [17]. RF magnetron sputtering has the advantage of a large throughput at small cost and a large uniform region; both properties are appropriate for industrial applications.

Artificial superlattices provide excellent opportunities to manipulate the strain and chemical heterogeneity so as to enhance properties. In previous work we evaluated an optimal growth condition to yield a $BiFeO_3/LaNiO_3$ (BFO/LNO) superlattice of enhanced crystal quality [18]. Based on the optimal growth conditions, we here report the effect of the sublayer thickness on the polarization of a BFO/LNO superlattice formed on a Nb-$SrTiO_3$ (STO) substrate with a RF magnetron-sputtering system; we investigated the effect of superlattice formation on the ferroelectric and leakage properties of BFO.

2. Experiments

A BFO/LNO superlattice was grown on a Nb-STO (001) substrate with an Ultra High Vacuum RF magnetron-sputtering system. The chamber was evacuated below 6.6×10^{-7} Pa to avoid contamination. For the BFO thin film, a $Bi_{1.2}FeO_3$ ceramic served as a target; the excess bismuth compensated for Bi volatilization during deposition [19]. The RF magnetron sputtering was performed at power density 0.74 W cm^{-2} (BFO) and 0.98 W cm^{-2} (LNO); the pressure of the gas was fixed at 2 Pa with Ar/O_2 ratio 4:1 and the growth rate was

* Corresponding author at: National Synchrotron Radiation Research Center, Hsinchu, Taiwan.
E-mail address: hylee@nsrrc.org.tw (H.-Y. Lee).
[1] Presenter: Yen-Ting Liu.

0040-6090/$ – see front matter © 2012 Elsevier B.V. All rights reserved.
doi:10.1016/j.tsf.2012.07.073

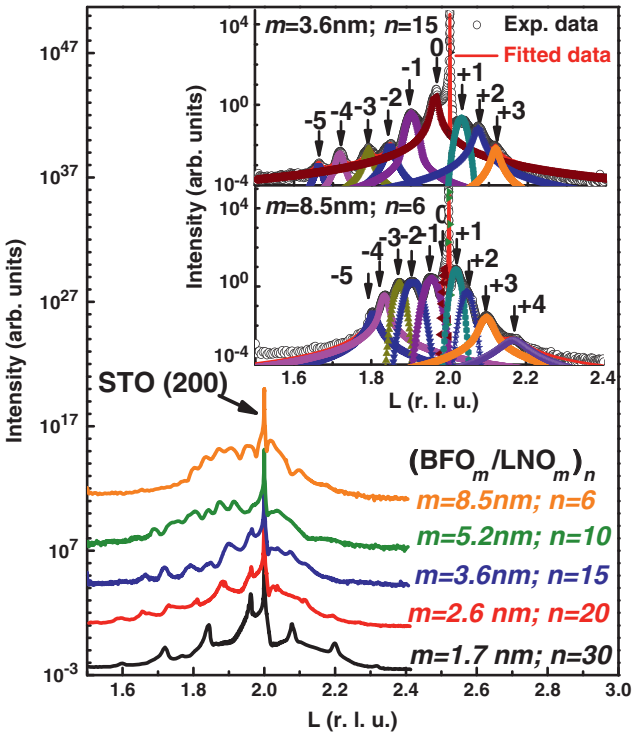

Fig. 1. Intensity distribution of a (002) radial scan of a BFO/LNO superlattice with varied thickness of sublayer and periods. The inset shows the best fits (solid line) to the experimental XRD patterns for BFO/LNO superlattices at thicknesses 3.6 and 8.5 nm of the sublayer.

0.6 nm/min (BFO) and 0.4 nm/min (LNO). A symmetric sublayer structure $(BFO_m/LNO_m)_n$, in which m is the thickness/nm of a sublayer and n is the number of repeating periods, was adopted. The superlattice structure contained BFO/LNO bilayers in 6–30 periods with the sublayer thickness in the range 1.7–8.5 nm at deposition temperature 660 °C. The total thickness of the films was fixed at ~100 nm.

With a synchrotron as a source of X-rays, we used high-resolution X-ray diffraction (HRXRD) to characterize the structure of the BFO/LNO heterostructure; these experiments were performed at wiggler beamline BL-17B1 in the National Synchrotron Radiation Research Center (NSRRC), Hsinchu, Taiwan. The composition of the depth profile was examined with a time-of-flight secondary-ion mass spectrometer (TOF-SIMS) and a Cs^+ ion source (12.5 keV with 50 nA current, CAMECA ims4f). The raster size was 250 μm × 250 μm and the sputtering rate was 0.06 nm/s. For the measurement of the ferroelectric properties and leakage current, a layer of Pt was deposited on top of the BFO/LNO superlattice through a shadow mask at 25 °C as a top electrode. The hysteresis loop of the polarization–electric field (P–E) of the BFO/LNO superlattice was measured with a ferroelectric test system (TF Analyzer 2000FE-Module, axiACCT Co.) at probing frequencies 0.5–1 kHz and voltage 6 V at 23 °C. The current density–electric field (J–E) curve was measured at voltage 3 V and current 1 mA; pulse-up pulse-down (PUPD) measurements were made with the same test system.

3. Results and discussion

Fig. 1, obtained from an eight-circle X-ray diffractometer and a high-resolution synchrotron source with a radial scan along direction (00L) of BFO/LNO superlattice films, shows the crystalline quality of the superlattice structure. The intense and sharp peak centered at $L=2$ is the STO (002) Bragg reflection from the substrate. The main peak (marked with arrows in Fig. 1) and well defined satellite lines on both sides of the main line indicate the great crystalline quality of the BFO/LNO artificial superlattice structure formed with RF magnetron sputtering. Expanded views of the fitted curve (solid line), using both symmetric and exponential composition profiles; experimental data (open circles) of BFO/LNO superlattice films with sublayers of thicknesses 3.6 and 8.5 nm in the inset of Fig. 1 indicate the position of the reflection of the satellite line (marked with an arrow). Overall, both assumptions yielded satisfactory agreement with the experimental data; some discrepancy of the background intensity near the substrate peak in the composition modulation shape is indicated by the satellite intensities. The superlattice exhibits satellite peaks that allowed us to deduce the super-period of the superlattice (Λ_{WAXRD}) according to the formula [20] $\Lambda_{WAXRD} = \frac{\lambda}{2(\sin\theta_n - \sin\theta_{n-1})}$, in which λ is the X-ray wavelength and θ_n and θ_{n-1} are the angular positions of two successive satellite lines. The period of the superlattice films obtained from the oscillations of the (002) radial scan shown in Table 1 agrees with the result of the X-ray reflectivity measurement. To verify the vertically periodic modulation obtained from the X-ray measurements, we examined the vertical composition profile of the BFO/LNO superlattices with SIMS. A SIMS depth profile of the $(BFO_{8.5}/LNO_{8.5})_6$ superlattice is shown in Fig. 2. The variations in the signals of Bi, Fe, La, Ni, Sr, Ti and O are consistent with the designed period of 6 cycles of a BFO/LNO superlattice. The total thickness obtained from the SIMS is consistent with the calculated value from the (002) radial scan and the X-ray reflectivity curve shown in Table 1.

The epitaxial relation between the BFO and LNO layers in the superlattice was examined according to the orientation in plane with respect to the major axes of the STO (001) substrate. The distribution of the X-ray intensity of an in-plane radial scan of the BFO/LNO superlattice film is shown in Fig. 3. The Bragg peak of the superlattice is shifted to a smaller H index and broadens rapidly with increasing thickness of the sublayer. The azimuthal diffraction patterns of a $(BFO_{1.7}/LNO_{1.7})_{30}$ superlattice in the vicinity of a surface peak and the substrate Bragg peak that clearly exhibits a four-fold symmetry with the same orientation appear in the inset of Fig. 3. These results constitute firm evidence for strong epitaxy of the deposited layer on the substrate. No other signals are observed in the intervals between the four peaks, indicating a perfect alignment of a and b axes of the BFO and LNO unit cells along those of the STO substrate.

The lattice parameters of BFO and LNO are 0.3962 and 0.3861 nm, respectively. The BFO sublayer is in a biaxially compressive state, whereas the LNO sublayer is in a biaxially tensile state in the

Table 1
Thickness parameters of a BFO/LNO superlattice obtained from the results of X-ray diffraction, X-ray reflectivity and SIMS.

Nominal sample	Λ_{WAXRD}/nm		Fitted thickness by X-ray reflectivity/nm			Total thickness (SIMS)/nm
	Modulation length $t_{BFO}+t_{LNO}$	Total thickness	t_{BFO}	t_{LNO}	Total thickness	
$(B_{1.7}/L_{1.7})_{30}$/STO	3.40 ± 0.17	102.0	1.70 ± 0.04	1.75 ± 0.04	103.5	
$(B_{2.6}/L_{2.6})_{20}$/STO	5.40 ± 0.27	108.0	2.60 ± 0.06	2.60 ± 0.06	104.0	
$(B_{3.6}/L_{3.6})_{15}$/STO	7.20 ± 0.36	108.0	3.08 ± 0.07	4.00 ± 0.10	106.2	
$(B_{5.2}/L_{5.2})_{10}$/STO	10.40 ± 0.52	104.0	5.30 ± 0.13	5.30 ± 0.13	106.0	104.0 ± 1
$(B_{8.5}/L_{8.5})_6$/STO	17.50 ± 0.88	105.0	8.70 ± 0.21	8.70 ± 0.21	104.4	105.0 ± 1

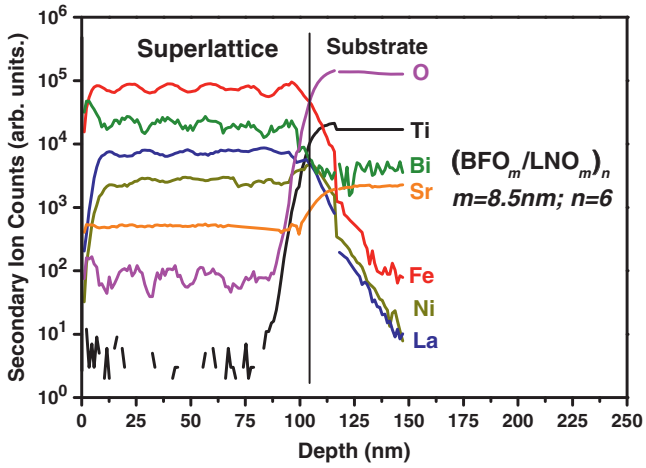

Fig. 2. SIMS depth profile of a $(BFO_{8.5}/LNO_{8.5})_6$ superlattice film.

superlattice system. The critical thickness for misfit dislocations, estimated according to a model proposed by Matthews and Blakeslee [21], of the BFO/LNO superlattice was ~15 nm. The designed modulation length ($t_{BFO}+t_{LNO}$) of the superlattices was from 3.4 nm to 17 nm. The lattice parameter of BFO in plane was determined directly from the (2 0 0) reflection [22,23]. The compressive strain in plane is defined as $(a_{BFO}-a_{bulk-BFO})/a_{bulk-BFO}$, in which a_{BFO} is the lattice parameter of the strained BFO layer observed from the in-plane radial scan of the superlattice and $a_{bulk\text{-}BFO}$ is the lattice parameter of strain-free bulk BFO. Based on this derived lattice parameter, the strains evaluated in plane and out of plane of BFO layers are related with $\varepsilon_\perp = -\frac{2\nu}{1-\nu}\varepsilon_{//}$ [24], in which ν is Poisson's ratio, $\varepsilon_\perp$ is the out-of-plane strain and $\varepsilon_{//}$ is the in-plane strain, shown in Fig. 4 (a). The thinner is the sublayer, the larger is the in-plane compressive strain of the BFO sublayers.

Fig. 4 (b) shows the *J*–*E* curve of BFO/LNO superlattice films with sublayers of varied thickness, which indicates large leakage current

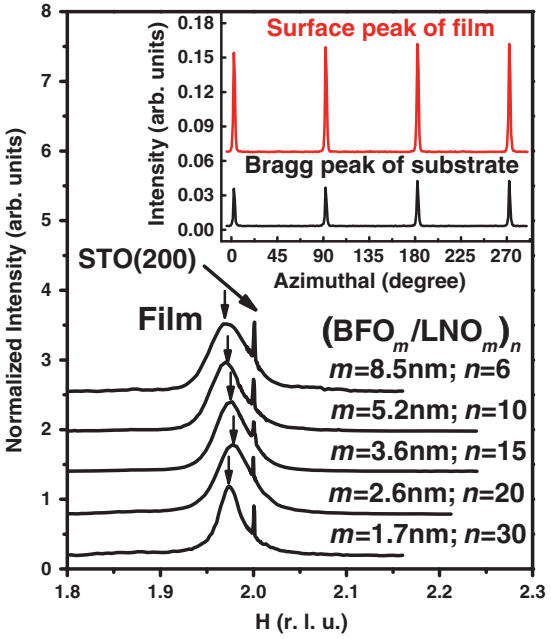

Fig. 3. X-ray intensity of a set of radial scans along the (200) in-plane Bragg line of BFO/LNO superlattice films deposited for varied periods. An arrow marks the position of the superlattice main peak. The inset shows an azimuthal scan (Φ scan) of the surface peak and the substrate Bragg peak for a $(BFO_{1.7}/LNO_{1.7})_{30}$ superlattice film.

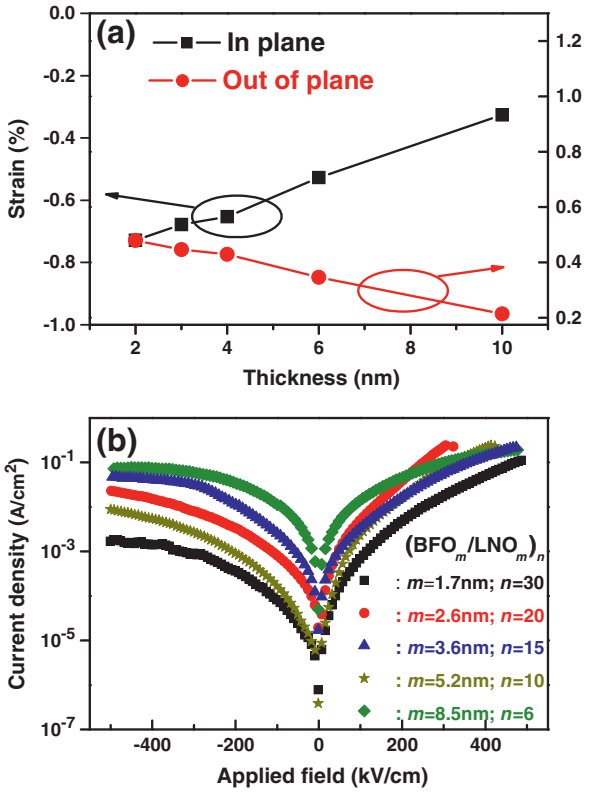

Fig. 4. Strain dependent and *J*–*E* curve of BFO/LNO superlattice films with varied sublayer thickness (a) in plane strain and out of plan strain, and (b) the *J*–*E* curve.

densities in this superlattice system for all periods; the leakage current increases with increasing thickness of the sublayers. In an insulating/conductive superlattice system, i.e., the BFO/LNO superlattice, there is a metallic layer in between, which increases the leakage current. An asymmetric feature of *J*–*E* curves might be due to varied Schottky barrier heights of the top and bottom electrodes or the varied extent of interface defects on both sides [25,26], which seem consistent with the tendency of the crystalline quality of the superlattice. The clearer diffraction peaks and satellite lines, the narrower diffraction in plane and the smaller mosaic structure of the film decrease the probability of leakage from the top electrode to the bottom electrode.

The ferroelectric properties of the BFO/LNO superlattice at thicknesses 1.7, 3.6 and 8.5 nm of a sublayer, and a BFO film of a single layer (thickness 60 nm), of the hysteresis loop of the polarization–electric field (*P*–*E*) are shown in Fig. 5. *P*–*E* hysteresis loops of BFO/LNO measured at probing frequencies 0.5–5 kHz and 25 °C show that both remanent polarization (P_r) and the coercive field (E_c) depend strongly on frequency. Hysteresis loops, with the largest remanent polarization ($2P_r$) near 160 μC cm^{-2}, were observed for $(BFO_{8.5}/LNO_{8.5})_6$ measured at 5 kHz. In the loops measured under 1 kHz, the contribution from the leakage is distinctly observable, as a result of which both the rounded shape and the remanent polarization increase; at frequency 2 kHz or greater, the contribution from the leakage was removed, and well saturated loops were observed. Despite the small dc leakage, the *P*–*E* loop was dominated by other effects of the extrinsic space charge, which might be due to the presence of a charged interface or defects or misfit dislocations formed through strain relaxation at the interface [27]. The poor ferroelectric nature of the BFO film can hence be attributed to the presence of mobile charge carriers (generated electrons and oxygen vacancies) at large concentrations [28]. Fig. 6(a) displays the variation with frequency of the polarization value ($2P_r$); at small probing frequencies, these mobile free charges contribute to the total polarization. The leakage is attributed to the presence of oxygen vacancies, which increase the amount of free carriers, leading to a degradation of the ferroelectric

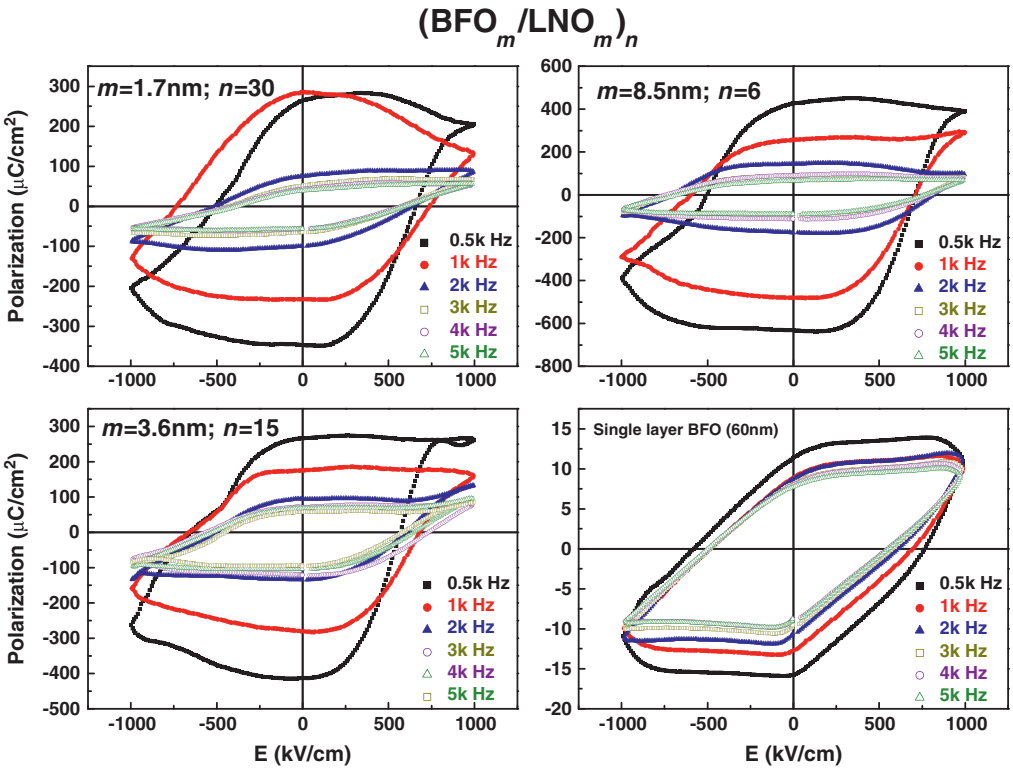

Fig. 5. *P–E* hysteresis loops of a BFO/LNO superlattice at thicknesses 1.7, 3.6 and 8.5 nm of sublayers and a BFO thin film of a single layer (thickness 60 nm).

properties [28]. The effect of the leakage current was much decreased on increasing the measurement frequency; the polarization value approached a saturation value at all sublayer thicknesses as shown in this figure. From the result of this polarization value, an effective strain manipulation of BFO sublayers in a superlattice structure by LNO sublayers can enhance the ferroelectric properties of the BFO sublayers. The interface was an issue of the ferroelectric property: the thinner is the sublayer, the greater is the extent of the interface in the superlattice; any imperfections at the interface, such as the formation of undesirable phases or electronic trapping states, seriously degrade the performance of the ferroelectric property [29]. For the same total thickness, the superlattice films of smaller sublayer thickness have more periods, and more interfaces result in a decreased effective thickness. The superlattice films that have a thicker sublayer with a diminished interface region therefore exhibited a larger remanent polarization. The value of remanent polarization (2 P_r) of the BFO layer, 2 P_r~160 μC cm^{-2}, obtained from Fig. 6(a) is eight times that, 2 P_r~20 μC cm^{-2}, for a single-layer BFO thin film (60 nm) prepared under the same sputtering conditions, at 660 °C and measured at 5 kHz. To confirm the polarization value of the superlattice, we performed a PUPD test with pulse width 0.25 ms and a delay 1000 ms. This pulsed measurement demonstrates that the measured polarization switching is an intrinsic property of the superlattice, and separate from the leakage property [11]. The results of the PUPD test are shown in Fig. 6(b); the remanent polarization obtained from the PUPD test was smaller than from the hysteresis loops but shows the same tendency with the result of the P–E loop, and likewise with the strain effect and the periods of the superlattice.

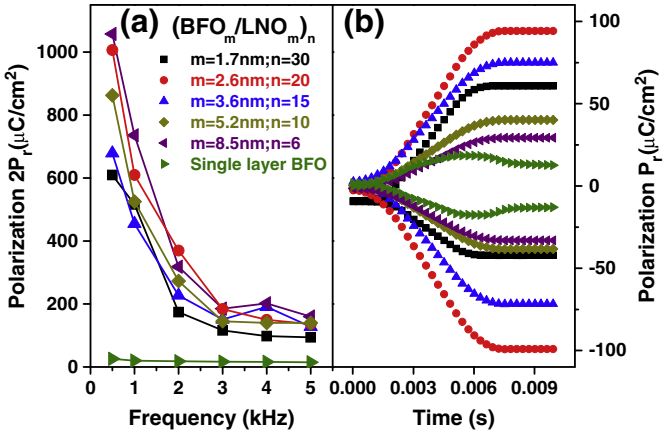

Fig. 6. Polarization measurements for all sublayer thicknesses and a single layer of BFO (a) polarization value (2 P_r) at varied frequency from *P–E* hysteresis loops, and (b) the remanent polarization obtained from the PUPD test.

4. Conclusions

For BFO/LNO superlattice structures fabricated on a Nb-doped STO substrate with a RF magnetron-sputtering system, we characterized the structure of the interface and the surface morphology of these films by measuring X-ray reflectivity and diffraction. An intrinsic remanent polarization of the superlattices was observed at the thickness of a sublayer in the range 1.7–8.5 nm at 5 kHz. The periods and thickness of the superlattice confirmed by XRD and XRR are consistent with the results of SIMS. The rounded shape of the hysteresis loop at frequency ≦2 kHz resulted from a large dc leakage and extrinsic interface effects.

Acknowledgment

National Science Council of the Republic of China provided support under contract NSC 99-2221-E-213-002-MY2.

References

[1] J. Wang, J.B. Neaton, H. Zheng, V. Nagarajan, S.B. Ogale, B. Liu, D. Viehland, V. Vaithyanathan, D.G. Schlom, U.V. Waghmare, N.A. Spaldin, K.M. Rabe, M. Wuttig, R. Ramesh, Science 299 (2003) 1719.
[2] G.A. Smolenskii, I. Chupis, Sov. Phys. Usp. 25 (1982) 475.
[3] M. Fiebig, J. Phys. D 38 (2005) R123.
[4] N.A. Hill, J. Phys. Chem. B 104 (2000) 6694.
[5] M. Dawber, K.M. Rabe, J.F. Scott, Rev. Mod. Phys. 77 (2005) 1083.
[6] J. Li, J. Wang, M. Wuttig, R. Ramesh, N. Wang, B. Ruette, A.P. Pyatakov, A.K. Zvezdin, D. Viehland, Appl. Phys. Lett. 84 (2004) 5261.
[7] C. Ederer, N.A. Spaldin, Phys. Rev. B 71 (2005) 224103.
[8] R.Y. Zheng, X.S. Gao, Z.H. Zhou, J. Wang, J. Appl. Phys. 101 (2007) 054104.
[9] H. Liu, K. Yao, P. Yang, Y. Du, Q. He, Y. Gu, X. Li, S. Wang, X. Zhou, J. Wang, Phys. Rev. B 82 (2010) 064108.
[10] J. Wang, H. Zheng, Z. Ma, S. Prasertchoung, M. Wuttig, R. Droopad, J. Yu, K. Eisenbeiser, R. Ramesh, Appl. Phys. Lett. 85 (2004) 2574.
[11] S.Y. Yang, F. Zavaliche, L. Mohaddes-Ardabili, V. Vaithyanathan, D.G. Schlom, Y.J. Lee, Y.H. Chu, M.P. Cruz, Q. Zhan, T. Zhao, R. Ramesh, Appl. Phys. Lett. 87 (2005) 102903.
[12] M. Kumar, V.R. Palkar, K. Srinivas, S.V. Suryanarayana, Appl. Phys. Lett. 76 (2000) 19.
[13] Y.Y. Kwi, D. Ricinschi, T. Kanashima, M. Noda, M. Okuyama, J. Appl. Phys. 43 (2004) L674.
[14] S.O. Park, C.S. Huang, H. Cho, C.S. Kang, H. Kang, S.I. Lee, M.Y. Lee, Jpn. J. Appl. Phys. Part 1 35 (1996) 1548.
[15] Y.C. Liang, Y.C. Liang, J. Cryst. Growth 285 (2005) 345.
[16] M. Matsuoka, K. Hoshino, K. Ono, J. Appl. Phys. 76 (1994) 1768.
[17] C.B. Eom, A.F. Marshall, S.S. Laderman, R.D. Jacowitz, T.H. Geballe, Science 249 (1990) 1549.
[18] Y.T. Liu, S.J. Chiu, H.Y. Lee, S.Y. Chen, Surf. Coat. Technol. 206 (2011) 1666.
[19] G.Z. Liu, C. Wang, C.C. Wang, J. Qiu, M. He, J. Xing, K.J. Jin, H.B. Lu, G.Z. Yang, Appl. Phys. Lett. 92 (2008) 122903.
[20] O.I. Lebedev, J.F. Hamet, G. Van Tendeloo, V. Beaumont, B. Raveau, J. Appl. Phys. 90 (2001) 5261.
[21] J.W. Matthews, A.E. Blakeslee, J. Cryst. Growth 27 (1974) 118.
[22] Y.C. Liang, T.B. Wu, H.Y. Lee, Y.W. Hsieh, J. Appl. Phys. 96 (2004) 584.
[23] U. Pietsch, H. Metzger, S. Rugel, B. Jenichen, I.K. Robinson, J. Appl. Phys. 74 (1993) 2381.
[24] H.H. Lee, M.S. Yi, H.W. Jang, Y.-T. Moon, S.-J. Park, D.Y. Noh, M. Tang, K.S. Liang, Appl. Phys. Lett. 81 (2002) 5120.
[25] K. Numata, Thin Solid Films 515 (2006) 2635.
[26] J. Wang, T. Zhang, J. Xiang, B. Zhang, Mater. Chem. Phys. 108 (2008) 445.
[27] S.P. Alpay, I.B. Misirlioglu, V. Nagarajan, R. Ramesh, Appl. Phys. Lett. 85 (2004) 2044.
[28] S. Bose, S.B. Krupanidhi, Appl. Phys. Lett. 90 (2007) 212902.
[29] S. Mathews, R. Ramesh, T. Venkatesan, J. Benedetto Sci. 276 (1997) 238.